

Original citation:

Vacheret, A., Barker, Gary John, Dziewiecki, M., Guzowski, P., Haigh, M. D., Hartfiel, B., Izmaylov, A., Johnston, W., Khabibullin, M. M., Khotjantsev, A. et al.. (2011)
Characterization and simulation of the response of Multi-Pixel Photon Counters to low light levels. Nuclear Instruments and Methods in Physics Research Section A: Accelerators, Spectrometers, Detectors and Associated Equipment, Vol.656 (No.1). pp. 69-83. ISSN 0168-9002

Permanent WRAP url:

<http://wrap.warwick.ac.uk/40100/>

Copyright and reuse:

The Warwick Research Archive Portal (WRAP) makes this work by researchers of the University of Warwick available open access under the following conditions.

This article is made available under the Creative Commons Attribution 3.0 Unported (CC BY 3.0) license and may be reused according to the conditions of the license. For more details see: <http://creativecommons.org/licenses/by/3.0/>

A note on versions:

The version presented in WRAP is the published version, or, version of record, and may be cited as it appears here.

For more information, please contact the WRAP Team at: wrap@warwick.ac.uk

warwick**publications**wrap

highlight your research

<http://go.warwick.ac.uk/lib-publications>



Characterization and simulation of the response of Multi-Pixel Photon Counters to low light levels

A. Vacheret^c, G.J. Barker^h, M. Dziewieckiⁱ, P. Guzowski^c, M.D. Haigh^{h,1}, B. Hartfiel^e, A. Izmaylov^d, W. Johnston^b, M. Khabibullin^d, A. Khotjantsev^d, Yu. Kudenko^d, R. Kurjataⁱ, T. Kutter^e, T. Lindner^a, P. Masliah^c, J. Marzecⁱ, O. Mineev^d, Yu. Musienko^d, S. Oser^a, F. Retière^{f,*}, R.O. Salih^g, A. Shaikhiev^d, L.F. Thompson^g, M.A. Ward^g, R.J. Wilson^b, N. Yershov^d, K. Zarembaⁱ, M. Ziembickiⁱ

^a Department of Physics & Astronomy, University of British Columbia, 6224 Agricultural Road, Vancouver, Canada, BC V6T 1Z1

^b Department of Physics, Colorado State University, Fort Collins, CO 80523, USA

^c Department of Physics, Imperial College London, South Kensington Campus, London SW7 2AZ, UK

^d Institute for Nuclear Research RAS, 60 October Revolution Pr. 7A, 117312 Moscow, Russia

^e Department of Physics and Astronomy, Louisiana State University, 202 Nicholson Hall, Tower Drive, Baton Rouge, LA 70803, USA

^f TRIUMF, 4004 Wesbrook Mall, Vancouver, Canada, BC V6T 2A3

^g Department of Physics and Astronomy, University of Sheffield, Hicks Building, Hounsfield Rd., Sheffield S3 7RH, UK

^h Department of Physics, University of Warwick, Gibbet Hill Road, Coventry CV4 7AL, UK

ⁱ Institute of Radioelectronics, Warsaw University of Technology, 15/19 Nowowiejska St., 00-665 Warsaw, Poland

ARTICLE INFO

Article history:

Received 10 January 2011

Received in revised form

18 June 2011

Accepted 12 July 2011

Available online 23 July 2011

Keywords:

Photosensors

Photodetectors

Multi-pixel avalanche photodiodes

Scintillator

ABSTRACT

The calorimeter, range detector and active target elements of the T2K near detectors rely on the Hamamatsu Photonics Multi-Pixel Photon Counters (MPPCs) to detect scintillation light produced by charged particles. Detailed measurements of the MPPC gain, afterpulsing, crosstalk, dark noise, and photon detection efficiency for low light levels are reported. In order to account for the impact of the MPPC behavior on T2K physics observables, a simulation program has been developed based on these measurements. The simulation is used to predict the energy resolution of the detector.

Crown Copyright © 2011 Published by Elsevier B.V. All rights reserved.

1. Introduction

The Tokai to Kamioka (T2K) project [1] is a second-generation long-baseline neutrino oscillation experiment that uses a high intensity off-axis neutrino beam produced by the 30 GeV proton beam at the Japan Proton Accelerator Research Complex (J-PARC). The first phase of the T2K experiment pursues two main goals: a sensitive measurement of θ_{13} , and determination of the parameters $\sin^2 2\theta_{23}$ and Δm_{23}^2 to better accuracy than any previous experiment.

To reach these physics goals, precise knowledge of the neutrino beam flux and spectrum, and the neutrino interaction cross-sections is required. To perform the required measurements, the near detector complex (ND280 [2]) was built at a distance of 280 m from

the hadron production target. The complex has two detectors (Fig. 1): an on-axis detector (neutrino beam monitor), and an off-axis neutrino detector located along the line between the average pion decay point and the Super-Kamiokande detector, at 2.5° relative to the proton beam direction. The on-axis detector (INGRID) consists of $7+7$ identical modules, arranged to form a “cross” configuration, and two “diagonal” modules positioned off the cross axes. The off-axis detector includes a magnet, previously used in the UA1 and NOMAD experiments, operated with a magnetic field of up to 0.2 T; a Pi-Zero detector (POD); a tracking detector that includes time projection chambers (TPCs) and fine grained scintillator detectors (FGDs); an electromagnetic calorimeter (ECAL); and a side muon range detector (SMRD).

The ND280 detector extensively uses scintillator detectors and embedded wavelength-shifting (WLS) fibers, with light detection from the fibers by photosensors that must operate in a magnetic field and fit in limited space inside the magnet.

After studying several candidate photosensors, a multi-pixel avalanche photodiode operating in the limited Geiger multiplication

* Corresponding author. Tel.: +1 604 222 7572; fax: +1 604 222 1074.

E-mail address: fretiere@triumf.ca (F. Retière).

¹ Current address: Department of Physics, The University of Oxford, Clarendon Laboratory, OX1 3PU Oxford, UK.

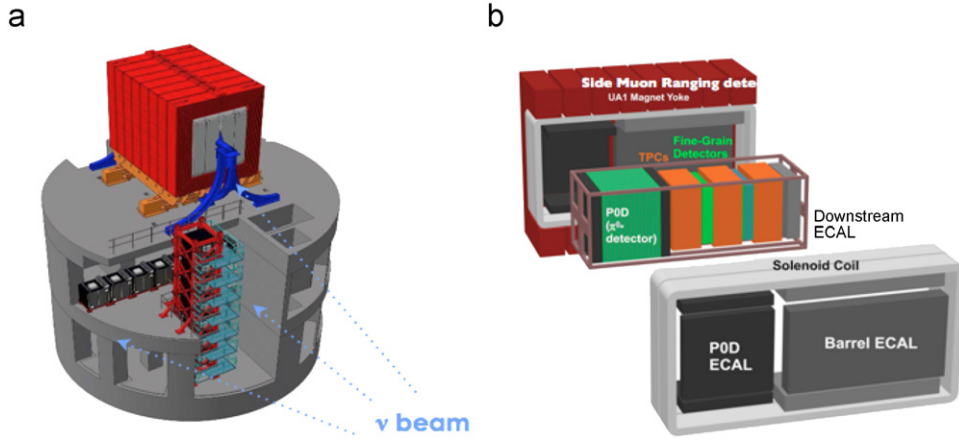


Fig. 1. Schematic view of (a) the T2K ND280 near detector complex consisting of the on-axis neutrino beam monitor (the “cross” configuration of cubical black modules on the two lower levels) and off-axis near neutrino detector on the top level, and (b) an exploded view of the off-axis near neutrino detector.

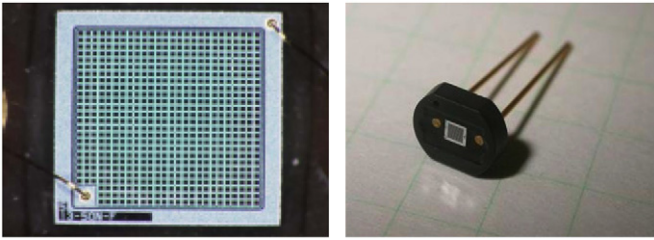


Fig. 2. Photographs of an MPPC with a sensitive area of $1.3 \times 1.3 \text{ mm}^2$: magnified face view (left) with 667 pixels in a 26×26 array (9 pixels in the corner are occupied by an electrode); the ceramic package of this MPPC (right).

mode was selected as the photosensor. These novel devices are compact, well matched to the spectral emission of WLS fibers, and insensitive to magnetic fields. Detailed information about such devices and basic principles of operation can be found in a number of papers [3–8] and references therein.

The operational parameters required for these photosensors were similar for all ND280 subdetectors and can be summarized as follows: an active area diameter of $\sim 1 \text{ mm}^2$, photon detection efficiency for green light $\geq 20\%$, a gain of $(0.5\text{--}1.0) \times 10^6$, more than 400 pixels, and a single photoelectron dark rate $\leq 1 \text{ MHz}$. The pulse width should be less than 100 ns to match the spill structure of the J-PARC proton beam. For calibration and control purposes it was very desirable to obtain well-separated single electron peaks in the amplitude spectra for dark noise and low light levels.

After an R&D study period of three years by numerous groups, the Hamamatsu Multi-Pixel Photon Counter (MPPC) was chosen as the photosensor for ND280. A description of this type of device and its basic parameters can be found in Ref. [9]. A customized 667-pixel MPPC with a sensitive area of $1.3 \times 1.3 \text{ mm}^2$ was developed for T2K [10]. It is based on the Hamamatsu commercial device S10362-11-050C with 400 pixels and $1 \times 1 \text{ mm}^2$ sensitive area. The sensitive area was increased to provide better acceptance of light from 1 mm diameter Y11 Kuraray fibers. In total, about 60,000 MPPCs were produced for T2K. The sensor is shown in Fig. 2.

In this paper, we present the results of measurements and simulations of the main parameters of Hamamatsu MPPCs developed for the T2K experiment, expanding upon the results given in Ref. [11]. Complementary results investigating the performances of the very similar $1 \times 1 \text{ mm}^2$ MPPC can be found in Ref. [12]. We emphasize the operational parameters of these devices most critical for successful operation and calibration of the T2K ND280

detectors: gain, dark rate, crosstalk, afterpulses and photon detection efficiency. This paper complements the results reported in Ref. [13], which focused on assessing the gross features of a large number of MPPCs. In this paper, dedicated setups were built to measure each process, which enabled more in-depth measurements than in Ref. [13] but in general these setups did not allow testing of a large number of MPPCs.

2. MPPC response

2.1. Operating principles

A Multi-Pixel Photon Counter consists of an array of avalanche photodiodes operating in Geiger mode. When operating in Geiger mode the diode is reverse-biased beyond the electrical breakdown voltage, which will be denoted V_{BD} throughout this document. Above V_{BD} , the electric field in the diode depletion region is sufficiently large for free carriers to produce additional carriers by impact ionization, resulting in a self-sustaining avalanche. In practice irreversible damage would eventually occur unless the avalanche is quenched. In MPPCs, quenching is achieved by using a large resistor in series with the diode. The current produced by the avalanche creates a voltage drop across the resistor (R_{quench}), which stops the avalanche when the voltage across the diode reaches V_{BD} . The overvoltage, denoted ΔV , is the difference between the operating voltage of the device and the breakdown voltage V_{BD} . The charge produced in an avalanche is hence the diode capacitance times ΔV . The above statement assumes that, given sub-nanosecond avalanche buildup time, the charge transferred through the quenching resistor during an avalanche is negligible with respect to the charge accumulated over the junction.

In Geiger mode, the amount of charge produced in an avalanche is independent of the number of charge carriers generated within the depletion region. Hence, it is not possible to measure the light intensity by measuring the total charge produced in a single avalanche. MPPCs achieve photon counting capability by segmenting the detection area in an array of individual diode pixels. The amount of light hitting the device is sampled by counting the number of pixels that produce avalanches, which leads to a saturation effect when a large amount of light hits the sensor. However, the focus of this paper is the MPPC response to low light levels, where the probability that multiple photons hit the same pixel at the same time is small.

The T2K MPPC is an array of 26×26 pixels, each of which measures $50 \times 50 \mu\text{m}^2$, on a common n++-type silicon substrate

[14]. Nine pixels in one corner have been replaced by a lead, reducing the total number of pixels to 667. The quenching resistors are polysilicon resistors. The Hamamatsu specifications sheet [9] states that the fill factor, i.e. the fraction of the device area that is active, is 61.5%. The breakdown voltage is about 70 V. When devices are purchased from Hamamatsu, rather than providing the breakdown voltage for each device, the voltage necessary to achieve a gain of 7.5×10^5 at 25 °C is provided.

2.2. Electrical properties

The total resistance and capacitance of an MPPC were measured using a picoammeter and capacitance–voltage (CV) analyzer, respectively. I – V and C – V plots are shown in Fig. 3. The MPPC capacitance was measured with a Keithley 590 CV analyzer. The capacitance drops rapidly with voltage down to -20 V, which presumably corresponds to the full depletion of the device. The capacitance of the MPPC was found to follow a linear relationship when the supply voltage is less than -20 V: $C_{\text{MPPC}} = aV + b$ with $a = 0.0436 \pm 0.0003$ pF/V and $b = 64.27 \pm 0.01$ pF. At -70 V, the capacitance is then 61.22 ± 0.02 pF. The Hamamatsu specification document for T2K's MPPCs states that the terminal capacitance is 60 pF, which is consistent with 61.28 pF obtained at -70 V operating voltage. In the remainder of this paper, the minus sign will be omitted when discussing operating voltage. Using 60 pF total capacitance and neglecting parasitic capacitance yields a pixel capacitance of $C_{\text{pix}} = 90.0$ fF.

The current was measured with a Keithley 617 programmable electrometer at 23 °C. A linear fit for a forward bias voltage larger than 0.6 V yields a slope of $R_{\text{quench}}/(667 \text{ pixels}) = 225 \Omega$. From this we determine the average quenching resistor value for this device to be $R_{\text{quench}} = 150 \text{ k}\Omega$; for a set of thirty five sensors this parameter was distributed in the range 148–154 k Ω . The current starts to increase dramatically at about -69 V bias voltage, which signals the beginning of the Geiger-mode region. The turnover is, however, not sharp and determining the breakdown voltage from the I – V curve requires using a function accounting for the transition from the linear to Geiger-mode regime, which was not attempted in this paper. The current increase slows down between -70 V and -71 V. Above -71 V, the current increases again very rapidly entering some sort of runaway mode, where avalanches trigger new avalanches continuously due to correlated noise, which will be described later on. Typically, MPPCs are operated at an overvoltage smaller than 2 V, corresponding to -71 V in this case. Hence, the current going through the device is less than 1 μ A.

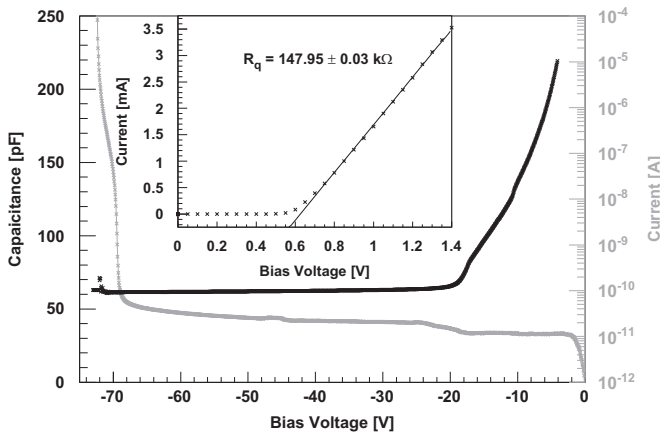


Fig. 3. I – V and C – V plots for an MPPC.

2.3. Recovery time

When an avalanche occurs in a pixel, the bias voltage across the diode drops down to the breakdown voltage. The diode voltage recovers to the nominal operating voltage with a time constant that is nominally given by the product of the pixel capacitance and the quenching resistor. Using the values of R_{quench} and C_{pixel} reported in the previous section, the recovery time constant is $\tau = 13.4$ ns. The overvoltage on the pixel at time t after the avalanche can then be written as: $\Delta V(t) = \Delta V(0)(1 - e^{-t/\tau})$, where $\Delta V(0)$ is the nominal overvoltage. We will see in the following section that the MPPC behavior is almost entirely driven by the overvoltage. Lower overvoltage implies a lower probability of triggering an avalanche. It also implies a lower MPPC gain, hence an avalanche occurring while the pixel is recovering will yield a lower charge.

The pixel voltage recovers to its nominal value by pumping charge from neighboring pixels and from the external electronics circuit. The typical equivalent circuit of silicon photomultiplier was introduced in Ref. [15]. The capacitance of one pixel (90 fF) is small compared to the total capacitance of the MPPC (60 pF). Hence the voltage drop induced by the avalanche in one pixel on all the other pixels is very small. However, the neighboring pixels effectively act as a bypass capacitor and the external circuit must eventually recharge the whole MPPC. The time constant introduced by the external circuit may be much longer than the pixel RC time constant and should be considered when investigating the response of the MPPC to large light pulses, or when the repetition rate of avalanches is high. Since here we focus on characterizing the MPPC response to low light levels (< 100 photoelectrons), the impact of the external electronics on the recovery time can be neglected.

2.4. Photosensor gain

The MPPC gain is defined as the charge produced in a single pixel avalanche, expressed in electron charge units. Single avalanches are typically created by a single carrier (unit charge) and can be triggered either by a photon or by thermal noise. Fig. 4 demonstrates excellent separation between the charges resulting from different number of photoelectrons. The gain is measured using a Multi-Channel Analyzer (MCA), by taking an amplitude spectrum and calculating the distance between the pedestal peak and the single photoelectron peak. Using other peaks provides consistent results. Conversion from the MCA output in digital counts to units of charge is achieved by calibrating the electronics with a known input charge. The calibration system was designed to mock up the MPPC current source, by sending a square wave

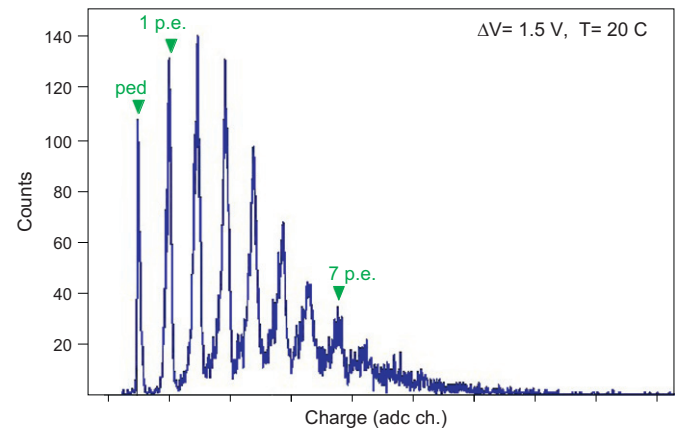


Fig. 4. A charge amplitude spectrum obtained using an LED source measured with an MPPC (serial number TA9445) at an overvoltage of 1.5 V and temperature of 20 °C.

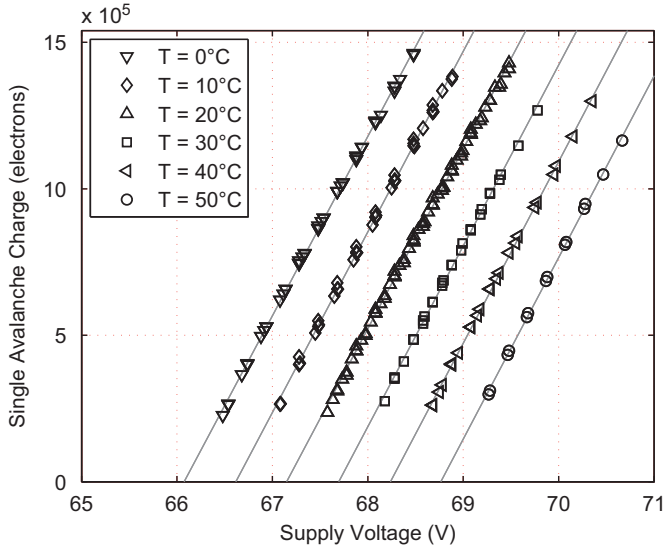


Fig. 5. MPPC gain vs. supply (bias) voltage at different temperatures (sensor serial number TA8120).

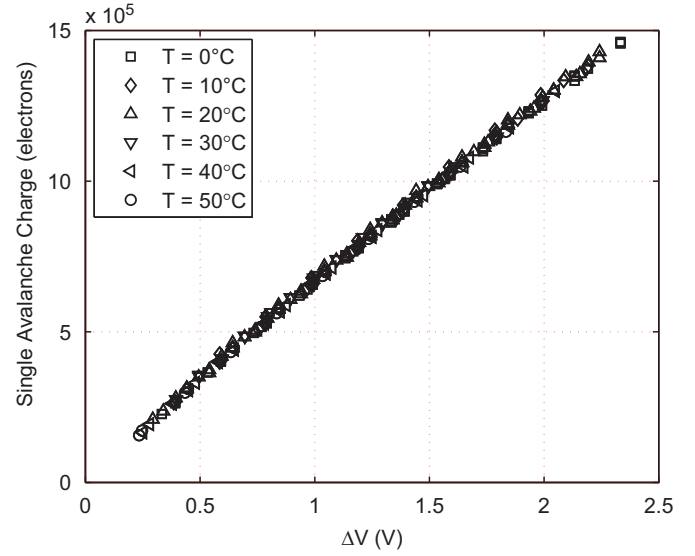


Fig. 6. Single pixel charge (gain) of an MPPC (serial number TA8120) as a function of the overvoltage ΔV at different temperatures.

into a 22 pF and adjusting the fall time with a set of resistors and capacitors to match the MPPC 13.4 ns RC time constant. The accuracy of the absolute gain measurement (i.e. the charge corresponding to a single avalanche) is affected mainly by the accuracy of the charge injection calibration. A description of the setup used for gain and subsequent dark rate measurement is given in Ref. [16].

Fig. 5 shows the gain as a function of operating voltage for various temperatures. The curves are fit by linear functions according to gain, $G = C_{\text{pix}}(V - V_{\text{BD}})$, where C_{pix} denotes the single pixel capacitance, V the operating voltage, and V_{BD} the breakdown voltage, which is measured by extrapolating the gain curves down to the point of zero gain. We note that the curves exhibit a slightly quadratic dependence, but a linear fit gives a reasonable estimate of V_{BD} and will be used throughout this paper. [We note that the voltage dependence of C_{MPPC} reported in Section 2.2 would cause the gain to have a quadratic dependence but this effect is smaller than the quadratic dependence we observe.] Since V_{BD} increases linearly by 52 ± 4 mV/°C, the gain decreases proportionately as the temperature increases at fixed operating voltage. However, the temperature variations within the T2K ND280 experiment are small enough that this effect can be calibrated out and does not require active compensation.

The overvoltage (ΔV) is calculated by subtracting the breakdown voltage from the operating voltage. Fig. 6 shows the single avalanche charge as a function of ΔV . The fact that the curves lie on top of each other shows that the temperature dependence of the gain is dominated by the temperature dependence of V_{BD} . The slopes of the curves are consistent with the 90 fF pixel capacitance estimated from the direct measurement, to within the equipment calibration accuracy. While it is not obvious in Fig. 6 due to the size of the symbols, individual fit of gain at each temperature shows a statistically significant 0.1% increase of the capacitance per degree at constant overvoltage, which can be attributed to a change in the permittivity of the silicon [17].

Fig. 4 shows that, unlike photomultiplier tubes, the MPPC gain fluctuations are significantly smaller than the charge from a single photoelectron avalanche. The gain fluctuations are, however, not negligible. The spectrum presented in Fig. 4 can be fit by a series of Gaussian distributions, with the μ parameter for each Gaussian representing the mean charge in the peak and σ its width due to gain fluctuations and electronics noise. The gain fluctuation

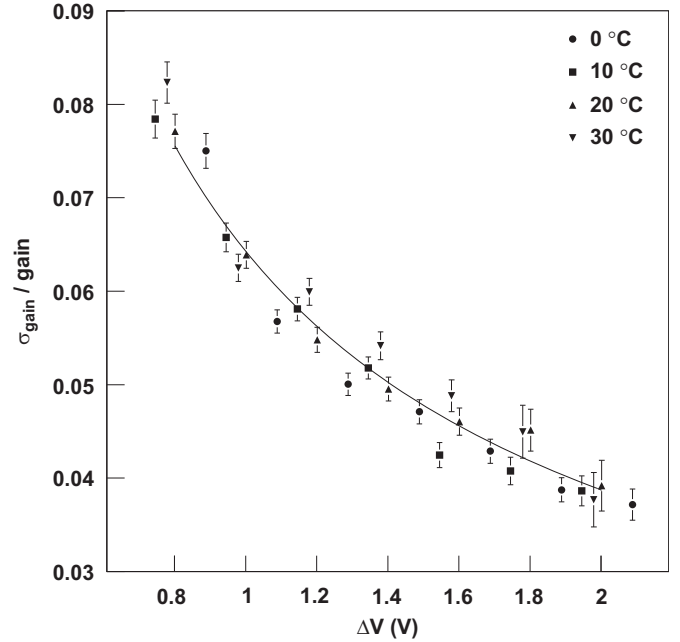


Fig. 7. Relative gain fluctuation vs. overvoltage at various temperatures. The curve is a fit to the $T=20^\circ\text{C}$ data.

parameter $\sigma(i)$ of the i th peak is well described by the equation:

$$\sigma(i)^2 = \sigma_{\text{ped}}^2 + i \cdot \sigma_{\text{Gain}}^2 \quad (1)$$

where σ_{ped} is the width of the pedestal, which is entirely due to the electronics noise, and σ_{Gain} accounts for the gain fluctuations. Measurements of σ_{Gain} show that it increases slightly with overvoltage. However, the achievable photoelectron resolution is related to gain fluctuation relative to the measured gain, G , so in Fig. 7 we show the ratio

$$\frac{\sigma_{\text{Gain}}}{G} = \frac{\sqrt{\sigma(1)^2 - \sigma_{\text{ped}}^2}}{G} \quad (2)$$

as a function of overvoltage, where σ_{ped} is the pedestal width and $\sigma(1)$ is the width of the single avalanche peak.

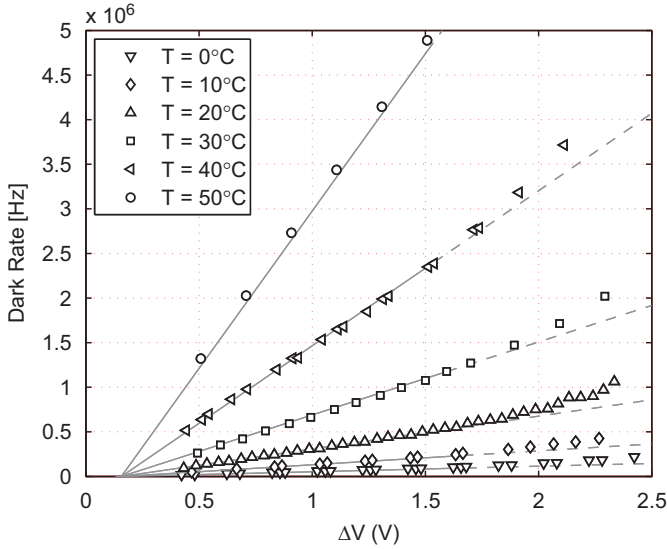


Fig. 8. Dark rate vs. overvoltage ΔV at different temperatures (sensor number TA8120). A single fit to Eq. (4) has been used to fit all the data points. Solid lines show results within the fit range ($\Delta V \leq 1.6$ V and $R_{DN} \leq 5$ MHz) while dashed lines represent extrapolations.

The 20 °C data can be parameterized by the following function: $\sigma_{\text{Gain}}/G = 0.064 \cdot \Delta V^{-0.73}$. The quality of the fit is good but we have no physical justification for this particular form. There appears to be a slight temperature variation, with the fluctuations being larger at higher temperatures.

2.5. Dark noise

Dark noise in Geiger-mode avalanche photodiodes is caused mainly by charge carriers generated thermally within the depletion region, which then enter the Geiger multiplication area and trigger avalanches. Any avalanche can, in turn, initiate secondary avalanches through afterpulsing and crosstalk. Thus, the dark noise consists of single pixel avalanche pulses, along with larger amplitude pulses generated by optical crosstalk, afterpulsing, and accidental pile-up from independent pixels. The last effect is negligibly small at dark rates below 1 MHz, assuming a short integration time at the MPPC output. Optical crosstalk and afterpulsing are discussed in the next sections.

Since most subsystems of our experiment acquire data as charge spectra within an integration gate associated with the beam crossing time, the relevant dark noise metric is the fraction of these gates populated by one or more dark pulses. The true rate of avalanches initiated by a single charge carrier can be obtained from a Poisson distribution,² using the following formula:

$$R_{DN} = -\ln\left(\frac{n_0}{N}\right)/\Delta t \quad (3)$$

where n_0 stands for the number of events with no counts, N for the total number of events, and Δt for the gate time. The measurements presented here used 160 ns gates triggered at a constant rate of 20 kHz.

Fig. 8 shows that the dark rate increases linearly with overvoltage in the range of 0.5–1.6 V. Above 1.6 V the points deviate upwards from the linear fit, which we attribute to an effect of afterpulsing. The temperature dependence is exponential and is

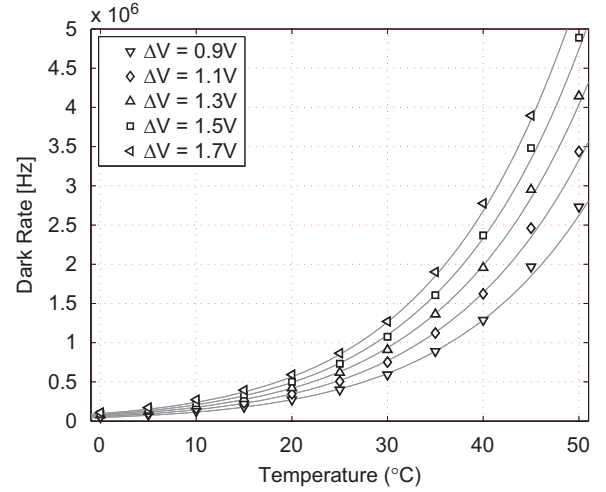


Fig. 9. Dark rate vs. temperature at different overvoltages ΔV (sensor number TA8120). A single fit to Eq. (4) has been used to fit all the data points, with the fit range restricted to $\Delta V \leq 1.6$ V and $R_{DN} \leq 5$ MHz.

shown in Fig. 9. The data for each sensor has been fit with a function of the form given in

$$R_{DN}(\Delta V, T) = A \cdot (\Delta V - V_0) \cdot \left(\frac{T}{298}\right)^{3/2} \cdot e^{-((E/2kT) - E/2k \cdot 298)} \quad (4)$$

where T is absolute temperature. In this formula A represents the ratio of dark rate to overvoltage at $T = 298$ K (25 °C) (in kHz/V). V_0 is an offset of breakdown voltage calculated from the dark rate with respect to that obtained from the gain measurements, and E the band gap energy. The offset is statistically significant. It suggests non-linear behaviour of the dark noise rate at low overvoltage. The fit range was restricted to $\Delta V \leq 1.6$ V and $R_{DN} \leq 5$ MHz, in order to avoid the effect of afterpulsing and rate limitations of the equipment.

The parametrization given in Eq. (4) has been obtained under following assumptions:

1. A non-degenerate semiconductor model was used.
2. Thermally generated charge carriers are a result of trap-assisted (i.e. involving an R-G center³) generation processes.
3. Given high reverse bias, the device operates in the so called ‘R-G depletion region’ steady state, i.e. no free charge carriers are available within the depletion region.
4. The trap energy level is close to the middle of the silicon’s bandgap.
5. Only processes occurring within the volume of the depletion region are taken into account. Surface generation/recombination is neglected.

Using such model, one can easily explain significant sensor-to-sensor variations of the dark rate by: (a) differences in the concentrations of traps (R-G centers) and (b) differences in dopant concentrations, hence different junction volumes. Mean value of the observed bandgap energy for the five measured sensors (Table 1) is 1.136 ± 0.0102 eV, which is within the range of values widely reported for silicon. Furthermore, reasonable χ^2/ν values and an average p -value of 46.8% do not provide enough evidence to reject the parametrization given by Eq. (4) at a statistically significant level, which is why we assumed that it can be used to approximate data from our measurements.

² Statistic associated with triggered elements in the MPPC is inherently binomial. However, given small number of triggered cells with respect to the total number of pixels, a Poisson distribution gives an excellent and convenient approximate.

³ Recombination-Generation center.

Table 1

Fit parameters for the dependence of the dark rate on ΔV and temperature. Eq. (4) was used with the fit range restricted to $\Delta V \leq 1.6$ V and $R_{DN} \leq 5$ MHz. A is the dark rate to overvoltage ratio at $T=298$ K (25 °C). V_0 is the difference between the breakdown voltage calculated from gain and dark noise. E is the band gap energy.

Sensor no.	A (kHz/V)	V_0 (mV)	E (eV)	χ^2/ν
TA8744	926 ± 5.8	149 ± 5.9	1.123 ± 0.0032	1.23
TA8160	555 ± 4.0	169 ± 6.4	1.146 ± 0.0042	1.04
TA8120	553 ± 3.3	159 ± 5.5	1.146 ± 0.0032	0.87
TA8092	615 ± 3.3	158 ± 4.9	1.133 ± 0.0030	0.76
TA9314	777 ± 5.2	151 ± 6.2	1.130 ± 0.0032	1.12
Mean			1.136 ± 0.0102	

The dark noise rate varies significantly between MPPCs as reported in Ref. [13]. A 20% variation in the dark noise rate was found at 20 °C and $\Delta V = 1$ V when calculating the variation as the root mean square (RMS) over the mean for the 17,686 tested MPPCs.

2.6. Afterpulsing

2.6.1. Correlated noise

Correlated noise is a general label for avalanches that are triggered by other avalanches. There are two known types of correlated noise: crosstalk and afterpulsing, both of which will be described and characterized in details in the next two subsections. In general, whenever an avalanche occurs there is a chance that it triggers one or more additional avalanches, either in neighboring pixels or in the same pixel at a later time. As mentioned earlier, the dark noise rate was estimated by counting the number of time no avalanches were detected within a gate. Indeed, the average number of avalanches detected within the gate is not a good estimator of the dark noise rate because some avalanches may have occurred due to correlated noise. Hence, in the presence of correlated noise, the measured average number of avalanches will exceed the expectation from Poisson statistics. Conversely, the measured number of events having one avalanche within the gate will be lower than the expectation. This fact can be used to get an estimate of the correlated noise.

The data used for measuring dark noise presented in the previous section can also be used to get an estimate of the correlated noise. From the dark noise rate measurement one can predict the fraction of events that should have one avalanche in the absence of correlated noise. The correlated event probability P_{CN} is the probability that one avalanche triggers at least one additional avalanche. The presence of this correlated noise term modifies the calculation of the number of events with one avalanche within the gate, N_1 , as follows:

$$\frac{N_1}{N_{tot}} = e^{-R_{DN}\Delta t} R_{DN}\Delta t (1 - P_{CN}) \quad (5)$$

where N_{tot} is the total number of events recorded, R_{DN} is the dark noise rate, and Δt is the gate width (160 ns). The correlated event probability is calculated by inverting this equation to obtain P_{CN} as a function of the measured quantities N_1 and R_{DN} (already shown in Fig. 8). P_{CN} is shown in Fig. 10 at different overvoltages and temperatures.

The temperature dependence is strikingly small. The data can be fitted by a quadratic function: $P_{CN} = k\Delta V^2$ with $k = 9.4 \pm 0.1\%$. The quadratic fit is good until $\Delta V > 1.6$ V, which is also approximately the overvoltage at which the measured dark noise rate no longer behaves linearly. As explained earlier, at sufficiently large overvoltage the method used to estimate dark noise becomes compromised by afterpulse avalanches that stem from dark noise avalanches prior to the integration gate. Hence, it is likely that the

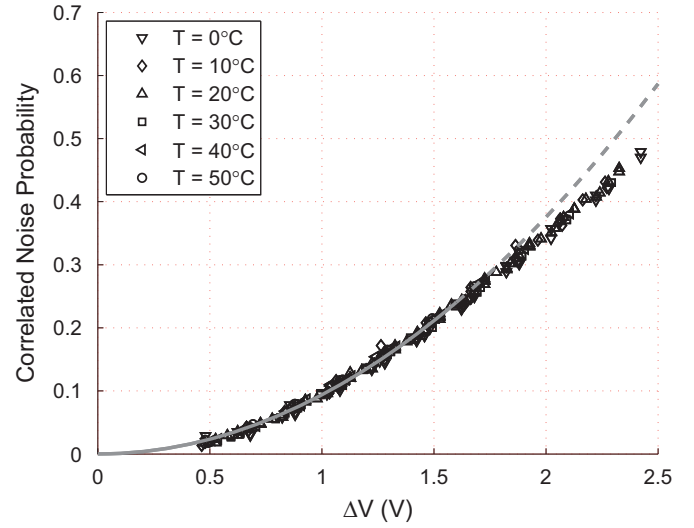


Fig. 10. Combined crosstalk and afterpulse probabilities vs. overvoltage at several temperatures.

failure of the fit results from the dark noise rate being incorrectly inferred when ΔV is greater than about 1.6 V.

2.6.2. Measuring afterpulsing

Afterpulsing is understood as being caused by the trapping of charge carriers created during an avalanche. The trapped carriers eventually get released and trigger an avalanche within the same pixel as the original avalanche, but delayed in time. Afterpulsing may be partially suppressed by the fact that the pixel voltage recovers in about 45 ns (a 13.4 ns time constant) as described in Section 2.3. If a carrier is released while the pixel voltage has not reached the nominal voltage, then the charge produced in the avalanche will be lower than for nominal avalanches. For a self-consistent description of the data, it is best to factorize recovery and afterpulsing phenomena, i.e. to measure the number of afterpulse avalanches per original avalanche regardless of the pixel voltage at the time of the afterpulse avalanche. Because there may be different types of traps in the silicon, there is no reason to assume that afterpulsing should follow a single exponential decay. In fact previous measurements on a similar MPPC [18] have shown that afterpulsing exhibits two time constants.

Two methods were used to measure afterpulsing. The methods complement each other since they effectively probe different afterpulsing time constants. Both rely on the fact that afterpulse avalanches are correlated in time with their parent avalanche.

The first method is based on the analysis of waveforms described in Ref. [18]. The waveforms were fit with a superposition of single avalanche response functions that allow separating pulses occurring within a few nanoseconds of one another. The probability of an avalanche occurring at time t after another avalanche can be parameterized as

$$P(t) = \left[1 - \int_0^t P_{AP}(x) dx \right] \cdot P_{DN}(t) + \left[1 - \int_0^t P_{DN}(x) dx \right] \cdot P_{AP}(t) \quad (6)$$

where P_{AP} and P_{DN} are the afterpulsing and dark noise probabilities. [We note that the formula in Ref. [18] is incorrect and should be replaced by this one.] Afterpulsing can be parameterized using two parameters: n_{AP} , the number of afterpulse avalanches created per original avalanche, and τ , the time constant of the exponential distribution governing the afterpulse generation. A drawback of this method is that the likelihood of uncorrelated dark signals (with a rate of 500–1000 MHz) in the waveform limits the sensitivity to afterpulsing time constants of less than about 100 ns. However, this

method is well suited for measuring small time constants (< 50 ns) as the pulse finding techniques allow detecting pulses separated by a few nanoseconds.

The second method is based on counting the number of avalanches with a scaler after introducing a controlled deadtime following each detected avalanche. The width of the analog pulse resulting from the convolution of the MPPC and amplifier response was such that the minimum deadtime that could be set was 26 ns. This minimum gate width means that this method is sensitive only to afterpulsing time constants of greater than about 50 ns. However, in contrast to first method, the counting technique overcomes the dark noise background limitation when measuring long time constants by taking very high statistics data. The deadtime dependent rate can be fit by a function that includes the contribution of dark noise and afterpulsing. In the absence of afterpulsing, the measured rate $R(\Delta t)$ for a given deadtime Δt is $R_{DN}/(1 + R_{DN}\Delta t)$. Afterpulsing produces avalanches that will increase the rate as long as they occur after the deadtime. To first order (i.e. assuming that one avalanche creates at most one additional detectable afterpulse avalanche and ignoring afterpulse avalanches created by previous afterpulse avalanches) the measured rate can then be calculated from:

$$R(\Delta t) = R/(1 + R\Delta t) \quad (7)$$

with (assuming two afterpulsing time constants)

$$R = R_{DN}/(1 - n_{AP0}e^{-\Delta t/\tau_0} - n_{AP1}e^{-\Delta t/\tau_1}) \quad (8)$$

where R_{DN} is the dark noise rate, n_{APi} ($i=0,1$) is the average number of afterpulse avalanches per original avalanche, and τ_i ($i=0,1$) the afterpulsing decay time constant.

Fig. 11 shows the afterpulse parameters for four different MPPCs measured at 25 °C using the waveform analysis technique. The probability is calculated from the number of afterpulse avalanches per original avalanche distributed as $1 - e^{-n_{AP}}$ and so is the probability that an avalanche generates at least one afterpulse avalanche. The exponential time constants were found to be $\tau_{short} = 17.6 \pm 2.1$ ns and $\tau_{long} = 71.4 \pm 8.3$ ns. The probabilities of “long” and “short” afterpulses are almost equal. The total probability of afterpulses is about 0.16 per initial avalanche at $\Delta V = 1.4$ V. The number of afterpulses per avalanche as a function of overvoltage can be fit by a simple quadratic function: $n_{AP}(\Delta V) = K \cdot \Delta V^2$, with $K_{short} = 0.0400 \pm 0.001(stat) \pm 0.005(sys)V^{-2}$ and $K_{long} = 0.0402(stat) \pm 0.001 \pm 0.005(sys)V^{-2}$. The dominant systematic error arises from the inability to detect pulses less than 2 ns after the first avalanche.

Fig. 12 shows the rate measured as a function of deadtime from 26 ns to 1 μ s at an overvoltage of 1.4 V at 25 °C. The fit to the data is excellent with an average χ^2 of 74.8 for 95 degrees of freedom. The fit parameters for the data from the MPPC shown in Fig. 12 yield $\tau_0 = 57 \pm 5$ ns, $n_{AP0} = 0.107 \pm 0.005$, $\tau_1 = 287 \pm 49$ ns, and $n_{AP1} = 0.043 \pm 0.006$. Repeating this test over 35 different MPPCs yield the following averages: $\tau_0 = 52(8)$ ns, $n_{AP0} = 0.105(0.009)$, $\tau_1 = 315(84)$ ns and $n_{AP1} = 0.066(0.01)$, with the standard deviations indicated in parentheses.

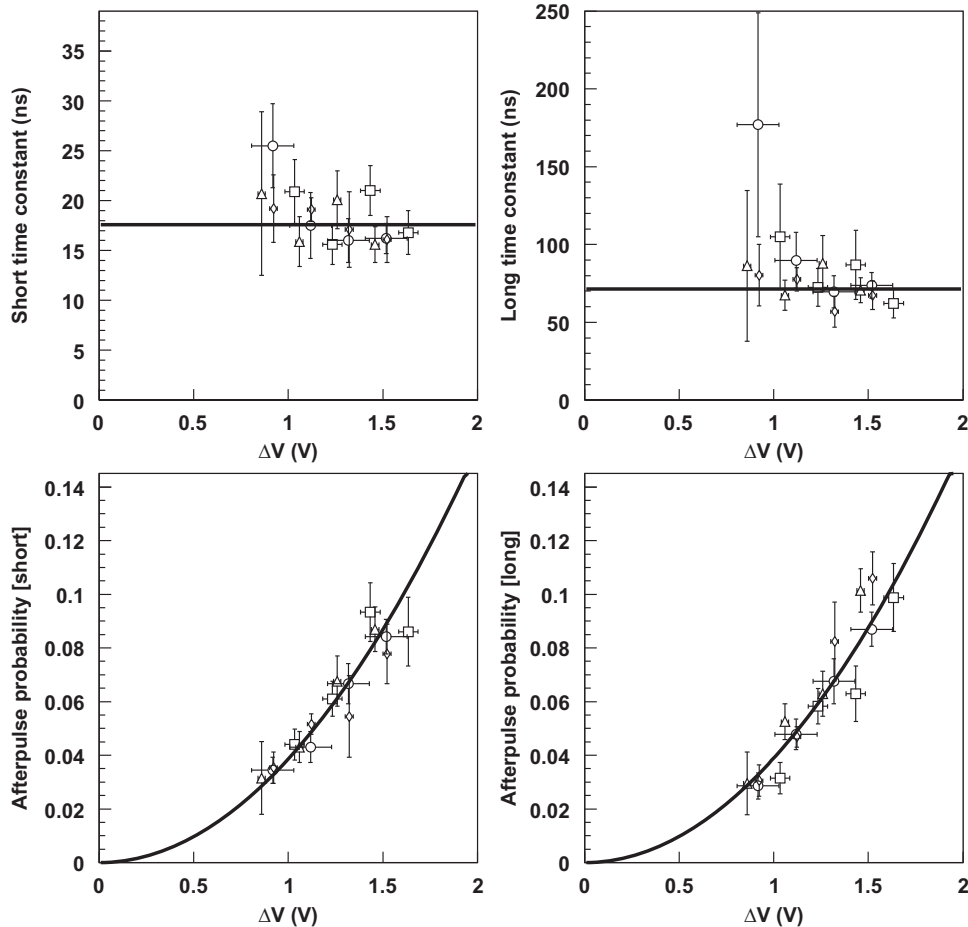


Fig. 11. Afterpulse parameters (exponential time constant and probability of having at least one afterpulse) vs. overvoltage for four different MPPCs (with plot symbols: square, circle, triangle, diamond) at 25 °C.

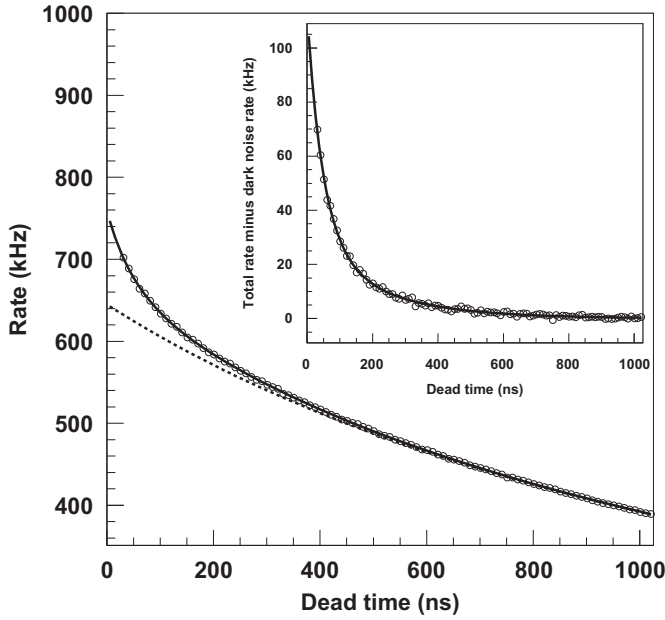


Fig. 12. Rate as a function of deadtime for an MPPC biased at 1.4 V overvoltage. The black curve shows a fit function including dark noise and two afterpulsing time constants. The dashed curve shows the estimated contribution of dark noise, i.e. the fit to Eq. (8) with afterpulsing probabilities turned off. The upper right inset shows the same data after subtracting the estimated dark noise.

Since the two measurement methods are sensitive to different afterpulsing time constant ranges it is not surprising they yield different results. It is possible to reconcile both methods by fitting the variable deadtime data for all MPPCs with three different afterpulsing time constants, two of them being fixed: $\tau_0 = 17$ ns and $\tau_1 = 70$ ns. The third time constant is a free parameter in the fit. Excellent fits are again obtained with an average χ^2 of 72.52 for 95 degrees of freedom, which is slightly better than the fit with just two time constants. The parameters averaged over the 35 MPPCs are $n_{AP0} = 0.058(0.03)$, $n_{AP1} = 0.090(0.008)$, $n_{AP3} = 0.056(0.009)$, and $\tau_3 = 373(55)$ ns, with the standard deviation among MPPCs in parentheses. The expectation from the waveform analysis at 1.4 V is $n_{APshort} = 0.078$ and $n_{APlong} = 0.082$. The introduction of this third (373 ns) time constant into the fitting function used for the waveform analysis at the level suggested by the variable deadtime analysis does not worsen the agreement with the data significantly and so is an acceptable additional parameter in a range not accessible to the method. Both analyses are also qualitatively consistent with the simple correlated noise analysis presented in the previous section, which predicts a total contribution of 0.184 for crosstalk and afterpulsing at $\Delta V = 1.4$ V.

The temperature dependence of afterpulsing was measured with the waveform technique for a couple of MPPCs at constant ΔV within a range of 13–25 °C as shown in Fig. 13. The amplitude of the “long” component of the afterpulsing rate is insensitive to temperature within measurement accuracy, the slope of the straight line fit being statistically consistent with zero. On the other hand, the amplitude of the “short” component decreases as the temperature

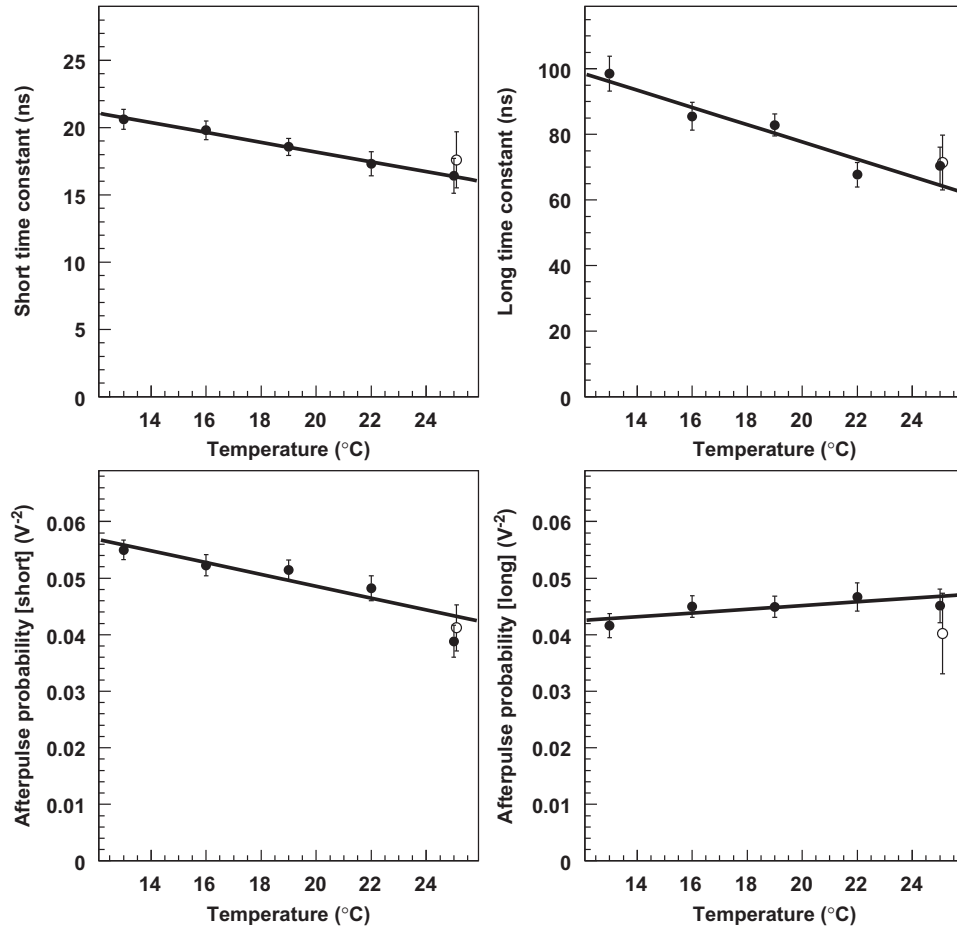


Fig. 13. Afterpulse parameters (exponential time constant and probability of having at least one afterpulse) vs. temperature.

increases with a coefficient of 2.0–2.5%/°C. The short and long time constants decrease with increasing temperature from 21 and 90 ns at 13 °C to 17 and 70 ns at 25 °C, respectively. In the MPPC simulation code, the temperature dependence of the 17 and 70 ns time constants is implemented, while the 370 ns time constant will be assumed to be constant since no temperature dependent data are available to quantify the variation. The measured time constants and their temperature dependence are consistent with Ref. [19].

2.7. Optical crosstalk

2.7.1. Crosstalk measurement

Optical crosstalk is believed to occur when optical photons produced in an avalanche propagate to neighboring pixels where they produce photoelectrons [20]. The result is that two or more pixels can be fired almost simultaneously (i.e. on a timescale of ≈ 1 ns). The photon emission probability has been measured to be on the order of $1\text{--}5 \times 10^{-5}$ photons per carrier crossing the junction [21,22], the absorption length for photons that are most effective in propagating the avalanches is typically 1 mm. Although the total crosstalk fraction is small, it is expected to vary with overvoltage and a detailed study is necessary to fully characterize local variations of the crosstalk phenomenon. Measurements of crosstalk variations within the pixel array as a function of voltage were performed using optical microscopy and waveform analysis.

2.7.2. Optical microscopy

Crosstalk probabilities were measured using the apparatus shown schematically in Fig. 14. A *nanoLED* [23] light source system was used to produce a pulse width of 1 ns FWHM from an integrated 463 nm LED. This was coupled to an optical fiber that terminated in a microscope lens such that the light beam is focused onto the MPPC face. The MPPC was mounted on an X–Y stage so that the beam spot could be translated across the MPPC pixel array with one micron position resolution. The MPPC signal was digitized with a 1 GHz sampling rate during a 1 μ s period using a Tektronix TDS 380 oscilloscope. The light pulse intensity was measured to be between 10–20 photons at the exit point of the fiber.

It was assumed that the amplitude of the avalanche signal observed is not dependent on the number of photons injected into a pixel if the photons all originate from the same LED pulse. Therefore, each LED flash creates a 1 p.e. signal as long as the beam spot is well-centered within a pixel. The trigger efficiency

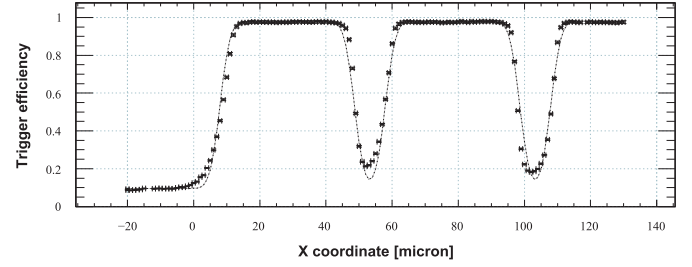


Fig. 15. MPPC detection efficiency across several MPPC pixels. The dashed line is the expected profile from the convolution of a Gaussian beam spot with $\sigma = 5 \mu\text{m}$ and square $50 \mu\text{m}$ pixels.

	Corner Pixel (Trigger pulse)			Side Pixel			In Array Pixel		
X	0.045	0.077	0.087	0.085	0.091	0.108	0.112	0.111	0.122
	0.045	0.065	0.073	0.069	0.084	0.097	0.126	0.123	0.115
	0.037	0.055	0.052	0.08	0.122	0.116	0.126	0.109	0.133
	Y			Y			Y		

Fig. 16. Measured crosstalk probabilities for nine beam positions inside an MPPC pixel at $\Delta V = 1.335$ V. (Left) a corner pixel with the corner located on the bottom left; (center) a side pixel with the side boundary to the left of the pixel and (right) a pixel inside the MPPC array. The thick black line denotes the limit of the pixel array.

was measured as the beam was scanned across several pixels to estimate the profile of the photon beam. The profile measured over $150 \mu\text{m}$ is shown in Fig. 15 and is consistent with a Gaussian beam spread of $5 \mu\text{m}$. The sensitive area is in good agreement with the value of 61.5% specified in the Hamamatsu catalog [9]. The non-zero baseline when X coordinate is less than $-10 \mu\text{m}$ is due to dark noise (0.1 avalanche for 1 μs integration time). This figure demonstrates that when the LED shines in the center of a pixel no light reaches neighbouring pixels.

2.7.3. Crosstalk study using waveform analysis

Waveforms were recorded for nine beam positions inside each of three pixels chosen for their specific position within the array, namely: a corner pixel, a side pixel and a pixel inside the MPPC array away from the edges. These pixels are surrounded by 3, 5 and 8 pixels, respectively, each of which may generate crosstalk signals. Crosstalk probabilities were calculated for individual photoelectron pulses selected to be within 8 ns after the LED trigger pulse. The total crosstalk probability is given by

$$P_{\text{ct}} = 1 - \frac{N(1 \text{ pe})}{N_{\text{tot}}} \quad (9)$$

where $N(1 \text{ pe})$ is the number of single 1 p.e. pulses and N_{tot} is the number of all LED pulses. The total crosstalk signal is defined as the observation of ≥ 2 p.e. pulses within the 8 ns time window, while individual crosstalk probabilities were extracted by selecting pulse heights corresponding to 2, 3 and 4 p.e. Data was taken for overvoltage $\Delta V = 1.335$ V and $T = 24^\circ\text{C}$; results for all three pixels are presented in Fig. 16. For all three pixels the crosstalk measured shows a clear dependence with position of the beam spot, suggesting that the crosstalk probability is correlated with where the photon is absorbed in the pixel. A similar analysis was applied to MPPC dark count data in a time window 500 ns before the LED triggers. The crosstalk was measured to be $9 \pm 1\%$ and no correlation with beam spot location was found.

Fig. 17 presents measurements of crosstalk probabilities as a function of overvoltage at $T = 24^\circ\text{C}$ for the same three pixels.

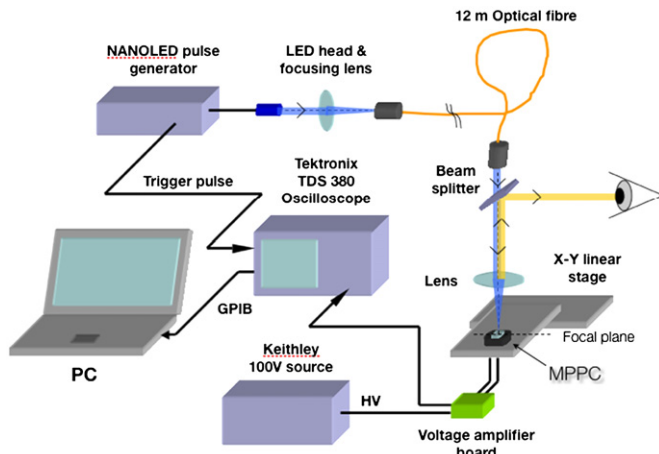


Fig. 14. Schematic of the optical microscopy apparatus used to measure MPPC crosstalk within a pixel.

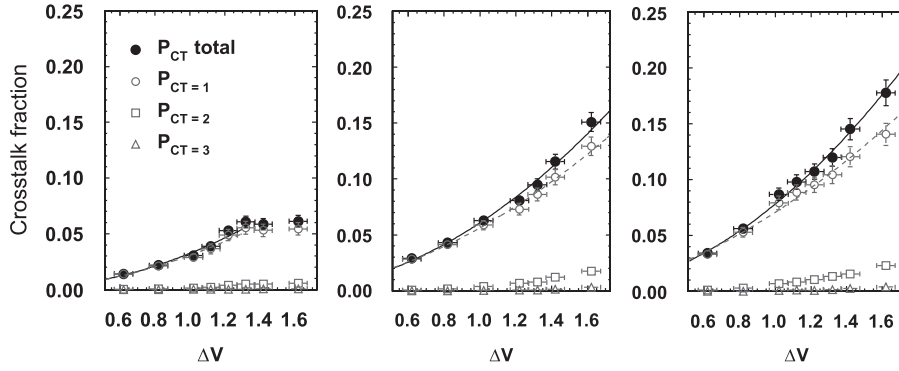


Fig. 17. Crosstalk value vs. overvoltage for three pixels shown in Fig. 16. P_{CT} is crosstalk probability, $P_{CT=1}$ is the probability of only one pixel fired in addition to the initial pixel, etc.

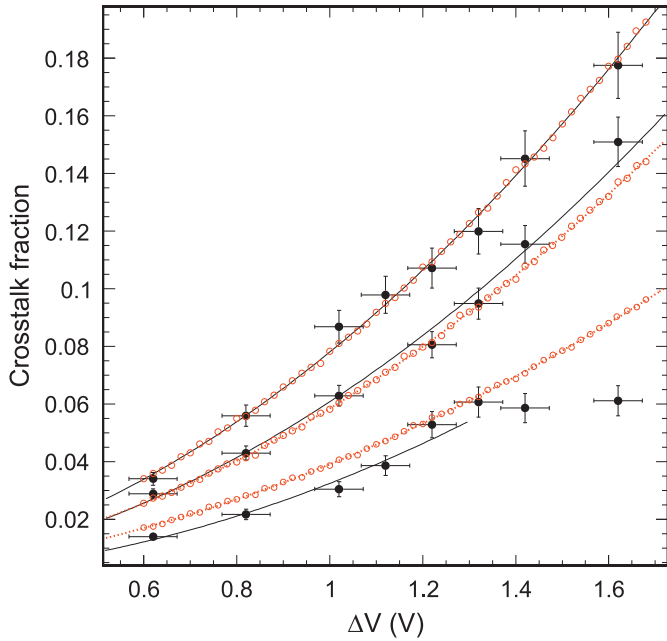


Fig. 18. Total crosstalk probabilities for all three pixels (corner, side and in-array). Data is shown as a solid circle, a solid black line indicates the best quadratic fit from Fig. 17. Simulated probabilities are shown as open circles and a dashed line.

Based on the position variation results, a correction factor is applied to correct the crosstalk probability to a probability averaged over the entire pixel. All probabilities were found to agree with a ΔV^2 dependence except for the corner pixels where the total probability plateaus at high overvoltage (above 1.3 V). This plateau is due to some peculiar behaviors of the corner pixels, which cannot be explained by geometrical considerations. Variations of the total crosstalk probability between pixels is qualitatively consistent with the hypothesis of a point source generation of optical photons in the pixel. The result of the crosstalk simulation is shown in Fig. 18 and agrees with the data for a nearest neighbor crosstalk hypothesis. This model is included in the simulation described in Section 3.

2.8. Photon detection efficiency

The photon detection efficiency (PDE) of a multi-pixel avalanche photodiode operated in a limited Geiger mode is a product of three factors:

$$PDE = QE(\lambda) \cdot \varepsilon_{\text{Geiger}} \cdot \varepsilon_{\text{pixel}} \quad (10)$$

where $QE(\lambda)$ is the wavelength dependent quantum efficiency, $\varepsilon_{\text{Geiger}}$ is the probability to initiate the Geiger discharge by a

carrier, and geometric acceptance $\varepsilon_{\text{pixel}}$ is the fraction of the total photodiode area occupied by the photosensitive area of the pixels.

For an MPPC, quantum efficiency can be defined as the probability for an incident photon to generate an electron–hole pair in a region in which carriers can produce an avalanche. The layer structure in an MPPC is optimized to have the highest probability for a visible photon to be absorbed in the depletion layer. For comparison, an APD with a similar layer structure to that of the MPPC developed by Hamamatsu for the CERN CMS experiment [24] has a measured quantum efficiency of more than 80% at 500 nm, so a similar value may be expected for the MPPC.

It is reasonable to assume that the device is fully depleted above breakdown voltage implying that the quantum efficiency has reached a maximum that depends only on wavelength and possibly incident angle. Hence, the overvoltage is expected to affect just one parameter in the expression, namely $\varepsilon_{\text{Geiger}}$. The breakdown probability depends on the impact ionization coefficients (for electrons and holes), which are strong functions of electric field. Simulation and measurements [25] show that $\varepsilon_{\text{Geiger}}$ behaves as the exponentially saturating function $\varepsilon_{\text{max}}(1 - e^{-k\Delta V})$ if breakdown is triggered by electrons. Breakdown initiated by holes leads to a linear dependence on ΔV .

The geometrical factor $\varepsilon_{\text{pixel}}$ is solely determined by the MPPC topology. Our measurements indicate $\varepsilon_{\text{pixel}} = 64\%$, which is consistent with the Hamamatsu specification of 62% for sensors with 50 μm pixels.

2.8.1. PDE measurement-pulsed LED method

For the PDE measurements we used an approach discussed in Ref. [26]. The PDE is measured using pulsed LED light with a narrow emission spectrum. The number of photons per LED flash is collimated to be within the MPPC sensitive area and reduced to an intensity that can fire only 2–5 pixels on average. The number of photons per LED pulse $N_\gamma(\lambda)$ can be measured using a calibrated photodetector, i.e. one with known spectral and single electron responses.

The PDE can be calculated from the recorded MPPC pulse height distribution (see Fig. 4) by assuming a Poisson distribution of the number of photons in an LED pulse. The mean value \bar{N}_{pe} of the number of photons recorded per LED pulse can be determined from the probability $P(0)$ of the pedestal (0 p.e.) events by $\bar{N}_{pe} = -\ln P(0)$. \bar{N}_{pe} calculated this way is independent of after-pulsing and crosstalk. Knowing the number of photons incident on the MPPC, $N_\gamma(\lambda)$, one can calculate $PDE(\lambda) = \bar{N}_{pe}/N_\gamma(\lambda)$.

The dependence of PDE on bias voltage was measured using a fast green emitting LED operating in a pulsed mode. The emission spectrum of this LED was measured to be very close to that of a Y11 WLS fiber. The peak value is centered around 515 nm, and it has FWHM of 40 nm.

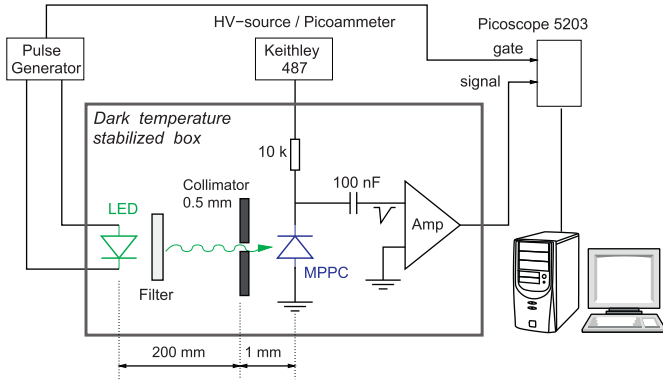


Fig. 19. Schematic diagram of the setup for the PDE measurements.

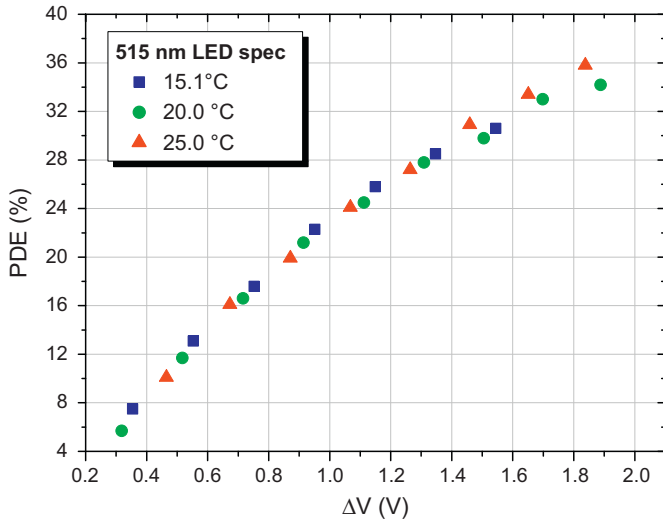


Fig. 20. Photon detection efficiency of a MPPC (serial number TA9445) for green light (~ 515 nm) as a function of overvoltage at three temperatures. (For interpretation of the references to color in this figure legend, the reader is referred to the web version of this article.)

The MPPC was illuminated with LED flashes through a 0.5 mm collimator (the distance between the LED and the collimator was 20 cm, and with about 1 mm between the collimator and the MPPC). A neutral density filter reduces the light intensity on the MPPC face to the level of 10–15 photons. The signal from the MPPC was amplified with a fast transimpedance amplifier and digitized with a Picoscope 5203 digital oscilloscope (250 MHz bandwidth, 1 GHz sampling rate). The signal integration time was 150 ns. A schematic diagram of the setup is shown in Fig. 19.

The PDE measurements were done in a temperature stabilized dark box ($\Delta T < 0.1^\circ\text{C}$). The number of photons in the LED flash was measured using a calibrated Hamamatsu photomultiplier R7899 ($\text{QE} = 15.7\%$ at 515 nm). The photoelectron collection efficiency for the 5-mm diameter central part of the photocathode is more than 95%, the PMT excess noise factor is 1.15. The LED amplitude spectrum measured for one of the tested MPPCs is shown in Fig. 4 at $\Delta V = 1.5$ V and 20°C .

The average number of photoelectrons in the LED signal was calculated by counting the number of pedestal events as discussed in Section 2.5. To correct for dark pulses that occurred randomly inside the 150 ns integration gate, the dark rate was measured during the same gate width but 300 ns earlier relative to the LED pulse. The stability of the LED pulse intensity was monitored and found to be better than $\pm 3\%$ during the measurements.

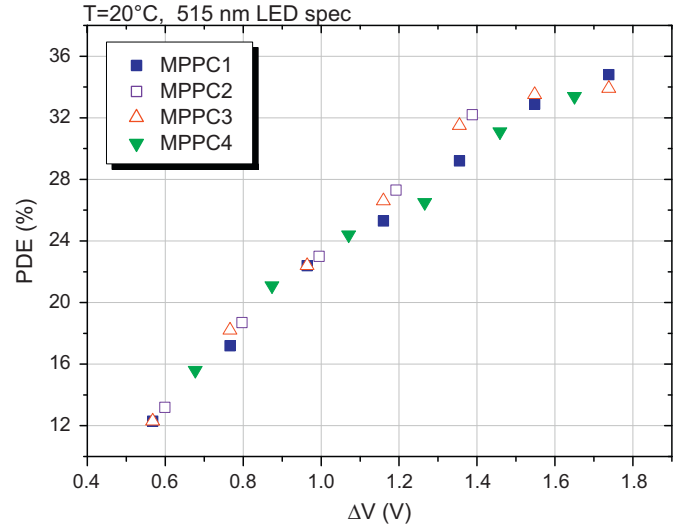


Fig. 21. PDE (at 515 nm) vs. overvoltage for four MPPCs at 20°C .

MPPC PDE as a function of overvoltage is shown in Fig. 20 for three temperatures. The PDE depends almost linearly on ΔV within the ΔV range of 1.0–1.6 V with slope of 1.5% per 100 mV. For a fixed overvoltage there is no observable dependence on temperature.

Fig. 21 shows the measured PDE for four additional MPPCs at 20°C . All show essentially the same performance with the PDE in the range 29–32% for green light at a typical operating overvoltage of 1.4 V. The measurement accuracy of the PDE is estimated to be about 10%. The largest contribution to this uncertainty is the normalization error, which is dominated by the error in the PMT spectral calibration (5–7%) followed by the uncertainty in the p.e. collection efficiency in the PMT (5%).

2.8.2. PDE measurement relative to an optical power meter

The PDE has also been measured independently using a 473 nm LED pulser developed as a calibration source for the ANTARES experiment [27] and with a 463 nm NanoLED pulser. The experimental setup is similar to that shown in Fig. 19. The MPPC signal was amplified with a gain of 40 and then sampled by a LeCroy WaveRunner 6100 oscilloscope (1 GHz bandwidth, 10 GSamples per sec) within a 200 ns gate. The temperature was held stable to 0.1°C by means of a thermally coupled metallic plate.

Calibration of the number of photons incident on the MPPC was performed using a Newport 1835-C Optical power meter with an 818 series 1 cm^2 photodiode sensor. The power meter converts an optical signal of specific wavelength into the optical power equivalent. The number of photons per flash can be calculated as follows:

$$N_\gamma = \frac{P_W \cdot \lambda}{F_{\text{Hz}} \cdot h c} \cdot A \quad (11)$$

where P_W is the measured optical power (in Watts) at wavelength λ (463 or 473 nm), F_{Hz} is the LED pulse rate (13 kHz), h is Planck's constant and A is an acceptance factor. Acceptance A is the ratio of intensity of LED light incident on the MPPC sensitive area to the intensity incident on the power meter sensor. The value of A is evaluated by performing a position scan of the LED light intensity profile.

The power meter calibration accuracy and the estimated acceptance factor are the dominant contributors to the uncertainties in the PDE measurement. As discussed in Section 2.8.1, the number of detected photoelectrons was obtained from the number of pedestal events in signal and assuming a Poisson distribution. The PDE values are free of afterpulsing and crosstalk contributions and were

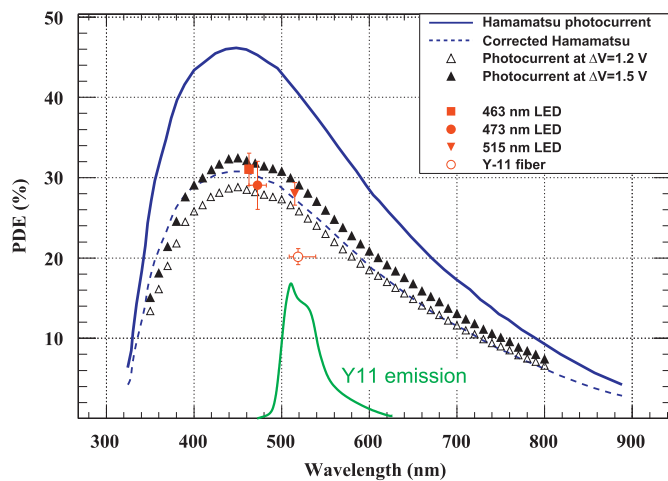


Fig. 22. MPPC PDE as a function of wavelength at $\Delta V = 1.2$ and 1.5 V at 25°C . Also shown is the spectral plot from the Hamamatsu catalogue, which uses data not corrected for crosstalk and afterpulsing (blue line); the dashed line is the Hamamatsu plot scaled-down using knowledge of the correlated noise contribution from our measurements. The green curve shows the Y11(150) Kuraray fiber emission spectrum (arbitrary units) for a fiber length of 150 cm (from Kuraray spec). LED and Y11 fiber points were measured at $\Delta V = 1.3$ V. (For interpretation of the references to color in this figure legend, the reader is referred to the web version of this article.)

corrected for dark rate. The PDE was found to be 31% for the 463 nm LED and 29% for the 473 nm LED at $\Delta V = 1.3$ V, which is in good agreement with the MPPC spectral sensitivity shown in Fig. 22 and discussed in the next section.

2.8.3. Spectral sensitivity

A spectrophotometer calibrated with a PIN-diode [26] was used to measure the spectral sensitivity of the MPPC. The spectrophotometer light intensity was reduced until the maximum MPPC current was only $\sim 30\%$ greater than the dark current to avoid non-linearity effects caused by the limited number of pixels. Comparing the MPPC current with the calibrated PIN-diode photocurrent we obtain the relative spectral sensitivity.

To achieve an absolute scale, the measured relative spectral response is scaled to the reference PDE points obtained with LED light at three wavelengths: 410, 460 and 515 nm measured at 1.2 V overvoltage. The scaling factor at other overvoltage values was found to be constant at these wavelengths up to about 1.4 V—the PDE spectral sensitivity shape is appreciably different above this, as was noted in Ref. [25]. The MPPC PDE dependence on the wavelength of the detected light along with the emission spectrum of the WLS Y11 Kuraray fiber are shown in Fig. 22. The MPPC peak sensitivity is in the blue light region, around 450 nm.

Since the spectrum of light incident on the MPPC in the ND280 detectors is determined by the Y11 fiber emission spectrum and the wavelength-dependent attenuation in the fiber, a PDE measurement was performed by exciting a Y11 fiber with a 405 nm LED [28]. The blue light source was arranged so that only re-emitted green light could reach the photosensor after propagating through 40 cm of the fiber. The fiber was coupled directly to the MPPC with the same design of optical connector used in the ND280 ECAL and POD subsystems. At $\Delta V = 1.3$ V, the PDE was measured to be 21%, which is significantly lower than the 28% measured at the same overvoltage with light incident directly onto the MPPC. The lower value may be due to light loss at the interface between the coupler and the Y11 fiber.

Fig. 22 also shows the MPPC spectral sensitivity measured by Hamamatsu for a commercial MPPC S10362-11-050 device at 25°C . These data, taken from the Hamamatsu catalog, are not corrected for crosstalk and afterpulsing. The method Hamamatsu

used is basically the photocurrent method described above but with a monochromator to select the incident light wavelength. The number of incident photons is derived from a calibrated photodiode response and the number of detected photoelectrons is obtained by dividing the MPPC current by its gain and the charge on an electron and assuming a Poisson distribution of the number of photons per single flash. We have corrected the Hamamatsu result by scaling down the PDE values by 0.663. This scaling factor was chosen to fit the sensitivity curve at the points measured with LEDs; the renormalized Hamamatsu spectral plot shape is consistent with our results within measurement accuracy.

3. MPPC simulation

A Monte Carlo simulation of the MPPC was written in C++ to simultaneously handle all the processes described earlier. Similar models have been developed by other groups, being either analytical [29] or partially analytical [30]. Our simulation can be split into two main components—a set of models defining device behavior, and a procedural framework to initialize the model using input parameters, control the simulation and output the results. The framework will be discussed briefly first.

3.1. Simulation framework

The simulation is based on a list of potential triggers (incident photons, thermally generated carriers and crosstalk/afterpulses), which are processed in time order. The only state variables of the MPPC are the voltages across each pixel; the evolution of these voltages between triggers is handled by a recovery model. On initialization, a list of incident photons is given to the simulation as input, and thermal noise is generated at the appropriate rate $\text{DCR}(V_{\text{nom}})$ for a nominal operating bias voltage and temperature. These two sources form the initial list of potential triggers.

Each potential trigger is then processed in the following steps:

1. The voltages on all pixels are updated from their state after the previous trigger, using the recovery model and the elapsed time since the last processed trigger.
2. It is determined whether the pixel fires. The probability is equal to $\text{PDE}(V_{\text{pix}})$ for photons and $\text{DCR}(V_{\text{pix}})/\text{DCR}(V_{\text{nom}})$ for dark noise, to account for the lower DCR for a pixel with depleted voltage, relative to the nominal DCR used to generate the noise triggers.
3. If the pixel fires, a trigger is added to the list of output signals and its voltage is set to zero; the charge of the generated avalanche depends on the voltage of the fired pixel and it is smeared by a Gaussian resolution function. The afterpulse/crosstalk models determine whether further noise is generated, and, if applicable, the additional noise is inserted into the list of potential hits, in correct time order.

The reinsertion of correlated noise resulting from an initial trigger allows higher-order noise cascades to be dealt with in a simple and natural way. The final output is a list of avalanches with times and charges, which can then be processed by code appropriate to a specific readout circuit.

3.2. Physics models

The simulation relies on accurate models for the various effects present in the sensor. The characterization measurements described above have been used to determine appropriate models to use, and to tune model parameters.

The dark rate is parameterized as a linear function of bias voltage—the parameters for this function must be measured separately for each sensor since large variations between devices are observed. The PDE is modeled with a quadratic fit to the data in Fig. 20; variation with wavelength is not included. The mean number of short- and long-lived trapped carriers for afterpulsing, and the lifetime of the trapped states, are taken from the results of the waveform analysis method in Section 2.6. The crosstalk model is based on the data and the model described in Section 2.7. The data shown in Fig. 18 are well-described by a simple nearest-neighbor model that assumes crosstalk occurs only in the four nearest-neighbor pixels to the primary pixel. Crosstalk pulses are generated according to the probability measured from dark noise. The location of the crosstalk pulse is then chosen randomly among the four neighboring pixels. The pulse is discarded if it falls outside the MPPC active area.

The recovery model used is specific to the ND280 Trip-t-based electronics (TFB board [31]), it assumes recharging of the fired MPPC pixels from capacitances elsewhere in the readout electronics for each channel. Recovery does not significantly affect response at low light levels, however, so it will not be discussed in further detail.

3.3. Comparison with data

The simulation output has been compared to data taken using the ND280 Trip-t electronics and a fast-pulsed LED, with a gate length of 540 ns and the photosensor at a temperature of 22 °C. An adjustable lens was used to alter the intensity of light incident on the sensor. All the parameters used for the simulation were taken from the characterization measurements, but some tuning was required to reflect sensor-specific parameters, electronics effects and light-level uncertainties. The linear fit parameters for the sensor dark noise curve were measured and used in the simulation. Since an absolute calibration of the incident light level was not available, the mean incident photon number was calculated for 1.33 V overvoltage using the method described in Section 2.8.1. The absolute PDE in the simulation is therefore not tested by this comparison, but errors in the parametrization of PDE as a function of voltage will be evident. Finally, the spread in total event charge due to electronics noise, and the spread in avalanche gains, were determined from the measured peak widths at a low light level and 1.33 V overvoltage, and added to the simulation.

Histograms of integrated output charge are shown in Fig. 23, for data and simulation. Very good agreement is seen between the data and MC for a range of light levels and overvoltages. Some small discrepancies between data and MC are seen in the integer-binned histograms; however, these histograms depend on the exact peak positions, which must be determined in the data by fitting. They also depend sensitively on the exact shapes of the peaks, since for large peak widths, each integer bin contains some events which have migrated from neighboring peaks. No significant systematic difference is observed between data and MC.

3.4. Energy resolution

In most cases, the energy resolution of scintillator detectors is dominated by the photon counting statistics when the number of photoelectrons is low (less than about 100). However, the photosensor and electronics can impact the energy resolution in two ways: (1) constant noise background due to dark noise and electronics noise and (2) fluctuation in the charge detected per photoelectron. The energy resolution can be calculated fairly accurately in the case where the MPPC charge is integrated over a time window Δt as shown for example in Ref. [29]. Ignoring the

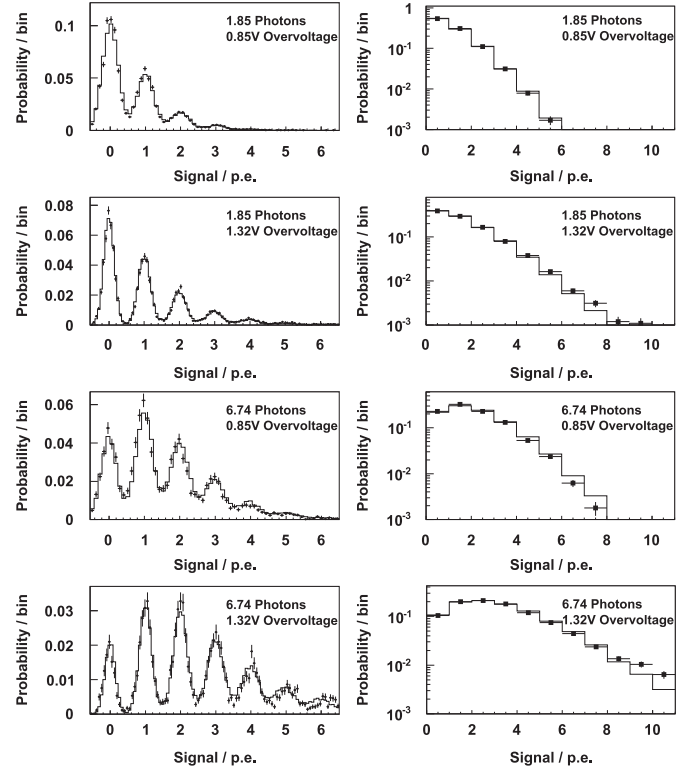


Fig. 23. Comparison of data to Monte Carlo at low light level for a range of overvoltages. The photon numbers shown are the number incident on the face of the MPPC. The histograms on the right show the same data as on the left, but with a bin width equal to the fitted peak separation in the data.

MPPC saturation effect, the standard deviation of the number of avalanches can be written as

$$\sigma_{N_{Av}}^2 = N_{Av} + N_{Av}\sigma_G^2 + \sigma_{el}^2 + R_{DN}\Delta t \quad (12)$$

where N_{Av} is the number of pixel avalanches, σ_G is the gain fluctuation parameter, σ_{el} is the electronics noise integrated over Δt , and R_{DN} is the dark noise rate. N_{Av} is related to the number of photoelectrons at low light level by $N_{Av} = N_{PE}(1 + N_{CN})$, where N_{CN} the number of correlated noise avalanches per avalanche. This latter formula is an approximation as it does not account for gain recovery and correlated noise avalanche created by other correlated noise avalanches. However, the MC simulation includes both effects. Some conclusions can be drawn from this formula: (1) the integration gate (Δt) should be chosen so that $N_{Av} \gg R_{DN}\Delta t$ in order to ensure that dark noise does not contribute to the resolution and (2) the gain fluctuations do not contribute to the resolution significantly since σ_G is only about 10%. This last conclusion highlights a significant difference between MPPCs and PMTs or standard Avalanche Photodiodes (APDs), whose main contribution to the energy resolution arises from gain fluctuations.

The simulated energy resolution is shown in Fig. 24 as a function of overvoltage with and without correlated noise (crosstalk and afterpulse). A gate of 540 ns was used to integrate the charge. The light flash occurred 60 ns after the beginning of the gate and the photons were produced according to an exponential with a 7 ns time constant. The number of incident photons was set to 100 to match the average number of avalanches triggered by a minimum ionizing particle in T2K near detectors, which ranges between 20 and 35 avalanches. Without correlated noise the energy resolution would improve with increasing ΔV because of the increasing photodetection efficiency. The improvement is

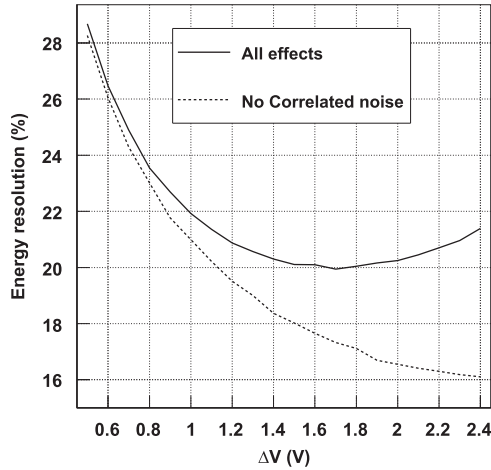


Fig. 24. Simulated energy resolution as a function of overvoltage for a typical MIP signal of about 25 avalanches. The confounding effects include crosstalk, dark noise and afterpulses. The curve without these effects includes only the variation of the MPPC efficiency with overvoltage.

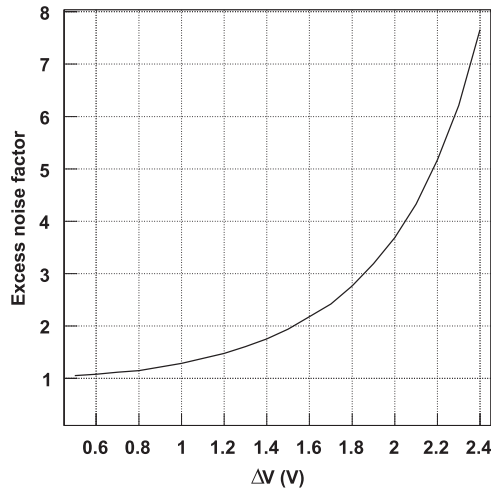


Fig. 25. Excess Noise Factor as a function of overvoltage.

expected to become marginal at large overvoltage as the PDE starts to saturate. In practice, when correlated noise is included the energy resolution reaches a minimum at $\Delta V = 1.8$ V. Beyond 1.8 V, correlated-noise-induced fluctuations worsen the energy resolution. Due to dynamic range constraints, in the T2K ND280 the MPPCs are operated at no more than $\Delta V = 1.33$ V.

The detector energy resolution is dominated by the photon counting statistics when ΔV is less than about 1.5 V; above 1.5 V correlated noise contributes significantly. For photomultiplier tubes and APDs, the contributions of gain fluctuations and correlated noise to the energy resolution are often assessed by calculating the excess noise factor (ENF). This better quantifies the contribution of the photosensor and the electronics system to the resolution by dividing out the fluctuations introduced by the photon counting statistics:

$$ENF = \sigma_{N_{Av}}^2 / N_{PE}. \quad (13)$$

We note that our ENF definition includes more sources of noise (dark noise, electronics noise) than the standard ENF defined for PMTs and APDs. However, the comparison is nevertheless relevant because, as discussed earlier the contributions of dark noise and electronics noise to the energy resolution are usually negligible.

The dependence of the excess noise factor with overvoltage is shown in Fig. 25. The ENF increases with increasing overvoltage following the increase of crosstalk and afterpulsing, which add additional avalanches in a stochastic manner. The ENF reaches 2 at a value of ΔV of about 1.5 V. The MPPC ENF is nevertheless significantly smaller than for APDs, whose ENF is always larger than 2 [32]. Overall, the MPPC contribution to the energy resolution is small for minimum ionizing particles that typically yield between 20 and 40 avalanches on average, even for T2K sub-detectors operating at $\Delta V = 1.33$ V.

4. Conclusion

The T2K experiment ND280 complex of detectors uses a 667-pixel MPPC developed by Hamamatsu Photonics specifically for this experiment. It has a sensitive area of 1.3×1.3 mm² and a pixel size of 50×50 μ m²; the sensitive area is larger than those available previously and relaxes the mechanical tolerances required for coupling to the WLS fibers used extensively in the experiment. We have performed detailed investigation of these devices and have developed an accurate model of the MPPC response to low light levels (where saturation effects can be neglected).

MPPCs biased at the recommended Hamamatsu overvoltage (1.33 V) at $T=25$ °C are characterized by the following parameters: photodetection efficiency of 28% when illuminated with light at the peak of the Y11 fiber emission spectrum (515 nm); a typical gain of 7.5×10^5 ; the average dark rate is 700 kHz but can approach 1 MHz; the crosstalk and afterpulse probability are estimated to be 9–12% and 14–16%, respectively, with a combined total of 20–25%; and the recovery time constant of a single pixel is 13.4 ns. We note that the photodetection efficiency reported by Hamamatsu photonics in Ref. [9] is overestimated by about 40% because of the measurement technique includes correlated noise. With such parameters, the device achieve the desired 20% energy resolution for minimum ionizing particles, which yield on average between 20 and 40 avalanches in the various components of the T2K near detector. Furthermore, about 40,000 MPPCs were operated in the T2K neutrino beam in 2009–2010 and no significant reliability issues were experienced.

Modeling the MPPC response by parameterizing dark noise, afterpulses, photodetection efficiency, crosstalk and gain variation enables us to account for the contribution of the photosensor to the overall detector response accurately. The MPPC saturation effect should also be fully described by our simulations, but confirmation of this awaits additional controlled measurements for final validation.

Acknowledgments

This work was supported in part by the “Neutrino Physics” Program of the Russian Academy of Sciences, the RFBR (Russia)/JSPS (Japan) Grant #08-02-91206, Polish Ministry of Science and Higher Education, Grant number 35/N-T2K/2007/0, US Department of Energy Grants DE-FG02-93ER40788 and DE-FG02-91ER40617, National Sciences and Engineering Research Council of Canada, and the UK Science and Technology Funding Council (STFC).

References

- [1] Y. Itow, et al., hep-ex/0106019.
- [2] “T2K ND280 Conceptual Design Report”, T2K Internal Document, See also D. Karlen, Nucl. Phys. B (Proc. Suppl.) 159 (2006) 91; Yu. Kudenko, Nucl. Instr. and Meth. A 598 (2009) 289; arXiv:0805.0411 [physics.ins-det].
- [3] G. Bondarenko, et al., Nucl. Instr. and Meth. A 442 (2000) 187.
- [4] B. Dolgoshein, et al., Nucl. Instr. and Meth. A 563 (2006) 368.

- [5] V. Golovin, V. Saveliev, Nucl. Instr. and Meth. A 518 (2004) 560.
- [6] D. Renker, Nucl. Instr. and Meth. A 567 (2006) 48.
- [7] D. Renker, E. Lorenz, J. Instr. 4 (2009) P04004.
- [8] Z.Ya. Sadygov, et al., Nucl. Instr. and Meth. A 504 (2003) 301.
- [9] "MPPC specifications": http://sales.hamamatsu.com/assets/pdf/catsandguides/mppc_kapd0002e07.pdf.
- [10] M. Yokoyama, et al., Nucl. Instr. and Meth. A 610 (2009) 128 arXiv:0807.3145 [physics.ins-det].
- [11] F. Retière, et al., Nucl. Instr. and Meth. A 610 (2009) 378.
- [12] P. Eckert, H.-C. Schultz-Coulon, W. Shen, R. Stamen, A. Tadday, Nucl. Instr. and Meth. A 620 (2010) 217.
- [13] M. Yokoyama, et al., Nucl. Instr. and Meth. A 622 (2010) 567 arXiv:1007.2712 [physics.ins-det].
- [14] K. Yamamoto, et al., PoS PD07 (2007) 004.
- [15] F. Corsi, et al., Nucl. Instr. and Meth. A 572 (2007) 416.
- [16] M. Dziewiecki, R. Kurjata, J. Marzec, R. Sulej, K. Zaremba, M. Ziembicki, PoS PD09 (2009) 016.
- [17] J. Krupka, J. Breeze, A. Centeno, N. Alford, T. Claussen, L. Jensen, IEEE Trans. Microwave Theory Tech. 54 (2006) 3995.
- [18] Y. Du, F. Retière, Nucl. Instr. and Meth. A 596 (2008) 396.
- [19] S. Cova, A. Lacaita, G. Ripamonti, IEEE Electron. Devices Lett. ED-12 (1991) 685.
- [20] A. Spinelli, A.L. Lacaita, IEEE Trans. Electron. Devices ED-44 (1997) 1931.
- [21] A.L. Lacaita, et al., IEEE Trans. Electron. Devices ED-40 (3) (1993) 577.
- [22] R. Mirzoyan, et al., Nucl. Instr. and Meth. A 610 (2009) 98.
- [23] NanoLED, Jobin Yvon Ltd., 2 Dalston Gardens, Stanmore, Middlesex HA7 1BQ, UK.
- [24] K. Deiters, et al., Nucl. Instr. and Meth. A 442 (2000) 193.
- [25] D. Orme, et al., PoS PD09 (2009) 019.
- [26] Y. Musienko, et al., Nucl. Instr. and Meth. A 567 (2006) 57.
- [27] P. Amram, et al., Nucl. Instr. and Meth. A 484 (2002) 369.
- [28] M.A. Ward, A. Vacheret, Nucl. Instr. and Meth. A 610 (2009) 378.
- [29] S. Vinogradov, T. Vinogradova, V. Shubin, D. Shushakov, C. Sitarsky, IEEE Trans. Nucl. Sci. NS-58 (2011).
- [30] H.T. van Dam, S. Seifert, R. Vinke, P. Dendooven, H. Löhner, F.J. Beekman, D.R. Schaart, IEEE Trans. Nucl. Sci. NS-57 (2010) 2254.
- [31] J. Estrada, C. Garcia, B. Hoenison, P. Rubinov, "MCM II and the Trip chip", DO note 4009, Fermilab-TM-2226, 2003.
- [32] A. Karar, Y. Musienko, J.Ch. Vanel, Nucl. Instr. and Meth. A 428 (1999) 413.